

# Atomistic Structure Learning Algorithm with surrogate energy model relaxation

Henrik Lund Mortensen, Søren Ager Meldgaard, Malthe Kjær Bisbo, Mads-Peter V. Christiansen, and Bjørk Hammer\*  
*Department of Physics and Astronomy, Aarhus University, DK-8000 Aarhus C, Denmark.*

(Dated: October 7, 2021)

The recently proposed Atomistic Structure Learning Algorithm (ASLA) builds on neural network enabled image recognition and reinforcement learning. It enables fully autonomous structure determination when used in combination with a first-principles total energy calculator, e.g. a density functional theory (DFT) program. To save on the computational requirements, ASLA utilizes the DFT program in a single-point mode, i.e. without allowing for relaxation of the structural candidates according to the force information at the DFT level. In this work, we augment ASLA to establish a surrogate energy model concurrently with its structure search. This enables approximative but computationally cheap relaxation of the structural candidates before the single-point energy evaluation with the computationally expensive DFT program. We demonstrate a significantly increased performance of ASLA for building benzene while utilizing a surrogate energy landscape. Further we apply this model-enhanced ASLA in a thorough investigation of the  $c(4 \times 8)$  phase of the Ag(111) surface oxide. ASLA successfully identifies a surface reconstruction which has previously only been guessed on the basis of scanning tunnelling microscopy images.

## I. INTRODUCTION

Structure determination is a cornerstone in the development of new functional materials for applications as photo-voltaics, thermoelectrics, electrolytes, and heterogeneous catalysts<sup>1</sup>. Often, advances in creating new such materials are lead by experimental discoveries and subsequent characterization of the compounds serve to identify their precise structure and composition at the atomic scale. Once the structure of a material is known, its physico-chemical properties may be rationalized on theoretical grounds providing a basis for further improvements. The process of structure determination is highly non-trivial and is hampered by the rapid growth with problem size of both the configurational space and the cost of the individual first principles quantum mechanical computer calculations required.

A number of strategies for automated structural search have emerged. These include simulated annealing based on molecular dynamics (MD)<sup>2</sup> and stochastic search based on e.g. basin hopping<sup>3</sup> or even evolutionary algorithms<sup>4-9</sup>. The recent developments in machine learning (ML) techniques in chemical physics<sup>10</sup> have successfully been introduced to lower the computational demands for these search strategies. One method has been to model the potential energy landscape accurately with kernel based methods<sup>11-13</sup> or neural networks<sup>14-17</sup> so that many expensive energy and force evaluations necessary for the MD and the local relaxations can be circumvented. Typically, the machine learning models are trained on-the-fly with active learning protocols<sup>18-37</sup> and improved as more and more first-principles datapoints are accumulated. Other means for speeding up structural searches with machine learning have been the introduction of acquisition functions, based on Bayesian statistics, balancing exploration and exploitation<sup>38,39</sup>, the clustering analysis in the selection of evolutionary populations<sup>40</sup>, the estimation of local energies to guide mutation and cross-over operations in evolutionary searches<sup>41-43</sup>, and the construction of arti-

cially convex energy landscapes for initial relaxation of evolutionary candidates<sup>44,45</sup>.

Notwithstanding the considerable computational speedups that ML techniques have lead to in structural determination, the underlying search paradigm remains of stochastic nature. This means that as a catalogue of more and more likely structural candidates is constructed, no knowledge or understanding of the bonding mechanism is developed and identifying more candidates still relies on the element of chance. To tackle this issue, we have recently proposed the Atomistic Structure Learning Algorithm (ASLA)<sup>46</sup>, which uses neural network based image recognition and reinforcement learning to iteratively construct the most stable atomic structure given only the cell and the stoichiometry. ASLA is designed to develop a rational search strategy in which interatomic arrangements are introduced because they appear plausible based on prior data. ASLA reads discretized 2D or 3D image representations of molecular compounds and solids. It builds the next promising structure, conducts a single-point, i.e. an unrelaxed, first-principles energy calculation, and uses this new structure-stability datapoint to train the neural network.

In this work, we extend ASLA to include a surrogate energy landscape that is constructed on-the-fly. Whenever ASLA proposes a new structure, the structure is subjected to a computationally inexpensive local relaxation in the model before the computationally expensive first-principles single-point calculation is conducted. The method is shown to dramatically increase the performance of ASLA when applied to solving for the most stable  $C_6H_6$ -isomer, which is benzene. We further apply ASLA with surrogate model relaxations to the problem of finding the most stable geometry and stoichiometry of the Ag(111)  $c(4 \times 8)$ -phase surface, which has been experimentally and theoretically investigated in Refs. 47 and 48. Ag(111) oxide surfaces are known to be catalysts for the important ethene epoxidation reaction and have been studied for decades. Yet the structure of such systems

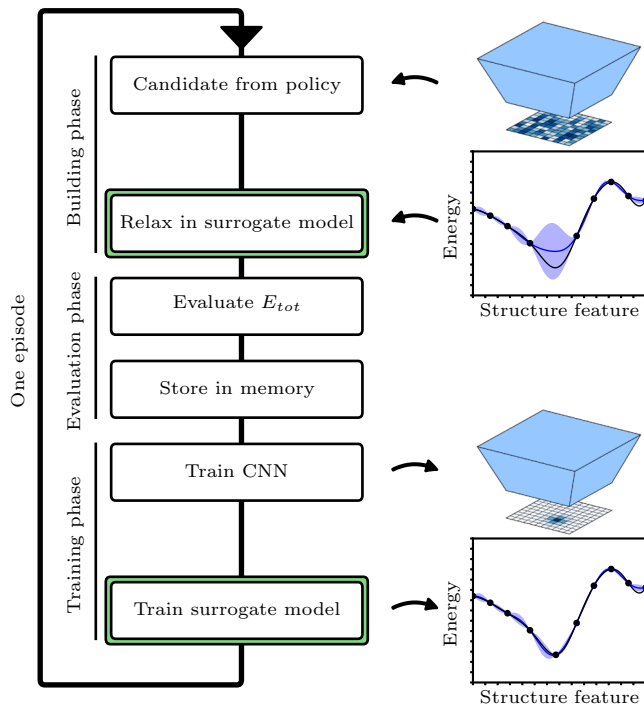


FIG. 1. Flowchart showing the three phases of ASLA. The green nodes highlight the contributions from this paper. The blue polygon represents the CNN producing the  $Q$ -value map, while the surrogate energy model, in which the relaxation is performed, is schematically represented as the blue curve in the structure-energy plot. The true energy curve is shown in black and black dots are training points, while the shaded area marks the model uncertainty. Both the CNN and the surrogate energy model improve in each episode, leaving ASLA better equipped for building low-energy structures in later episodes.

continue to surprise<sup>49</sup>. The important catalytic properties together with the rich structural diversity calls for reliable, automated global search algorithms for structure determination.

The paper is outlined as follows. In the first section, we introduce the details of the model. In the second section, we demonstrate the performance increase for a simple benzene system, where many restarts can be made and good statistics obtained. Lastly, in the final section, we employ our algorithm to identify the aforementioned Ag(111) oxide surface structure. Doing so, we employ the method for a large number of different silver oxide stoichiometries. The most stable structure is identified and discussed.

## II. ASLA

In the Atomistic Structure Learning Algorithm (ASLA)<sup>46,50,51</sup>, the global optimization problem of structure search is formulated as a reinforcement learning

problem, where an *agent* learns to build the most stable atomistic structure. The learning appears in *episodes*, in each of which, the agent itself creates a new prospective atomistic structure whose total energy is provided by an external density functional theory (DFT) program<sup>52,53</sup>. Each learning episode contains three distinct phases, the *building phase*, the *evaluation phase*, and the *training phase* as illustrated in the flowchart given in Fig. 1.

In the building phase, ASLA commences by constructing a new structural candidate by following the policy as guided by the current state of the agent. It starts from a *template* structure,  $s_0$ , (possibly an empty computational cell) and proceeds iteratively to a final state,  $s_T$ , such that a total of  $N_{\text{atom}}$  atoms have been placed, as further detailed in Fig. 2 a. In each iteration the intermediate state,  $s_t$ , is given to the agent equipped with a convolutional neural network (CNN), that responds with its expectation,  $Q(s_t, a_t)$ , of the reward for the most stable final structure attainable if *action*,  $a_t$ , is taken. An action is the combined information about position and type of the next atom to be placed, and a reward is a function whose maximum coincides with the most stable final structure found at any time, see Refs.<sup>46,50</sup> for details. With discretization of space, all possible actions for each type of atom can be represented on a 2D or 3D grid depending on the problem being solved. The expected rewards for all possible actions can hence be represented as  $Q$ -value maps on such grids. Discretized atomistic structures and  $Q$ -value maps thus share the same data structure as illustrated in Fig. 2 b. The  $Q$ -value maps form together with a *policy* the basis for a decision process regarding the actual action,  $a_t$ , taken at state  $s_t$  leading to state  $s_{t+1}$ . We employ a modified epsilon-greedy policy. This means that ordinarily it is the expected most rewarding action (greedy), which is chosen, but occasionally with some small likelihood (epsilon) a stochastic element is used in choosing the action<sup>46</sup>.

After constructing a candidate from the policy we add in the present version of ASLA a new element, namely a *structural relaxation*. The changes that a structural candidate undergoes during this are illustrated in Fig. 2 c. The structure relaxation seeks to identify the nearest local minimum energy structure in the vicinity of the structure just built. To avoid any significant computational expense of this operation, it is carried out in a surrogate energy landscape described in the next section. After completing the relaxation, the atom positions are adjusted slightly (snapped to grid) to ensure that the relaxed structure, now  $\tilde{s}_T$ , can be represented on the grid used for training the agent.

The reinforcement learning episode proceeds with the evaluation phase which is a single-point DFT calculation of the total energy,  $E_{\text{tot}}$ , of structure,  $\tilde{s}_T$ . This is the presumed computationally most intensive operation of the learning episode. Once finished, a set of state-action-energy datapoints for each iteration of the candidate-from-policy construction of this episode may be stored in the *memory* in the *store-in-memory event*. Since the candi-

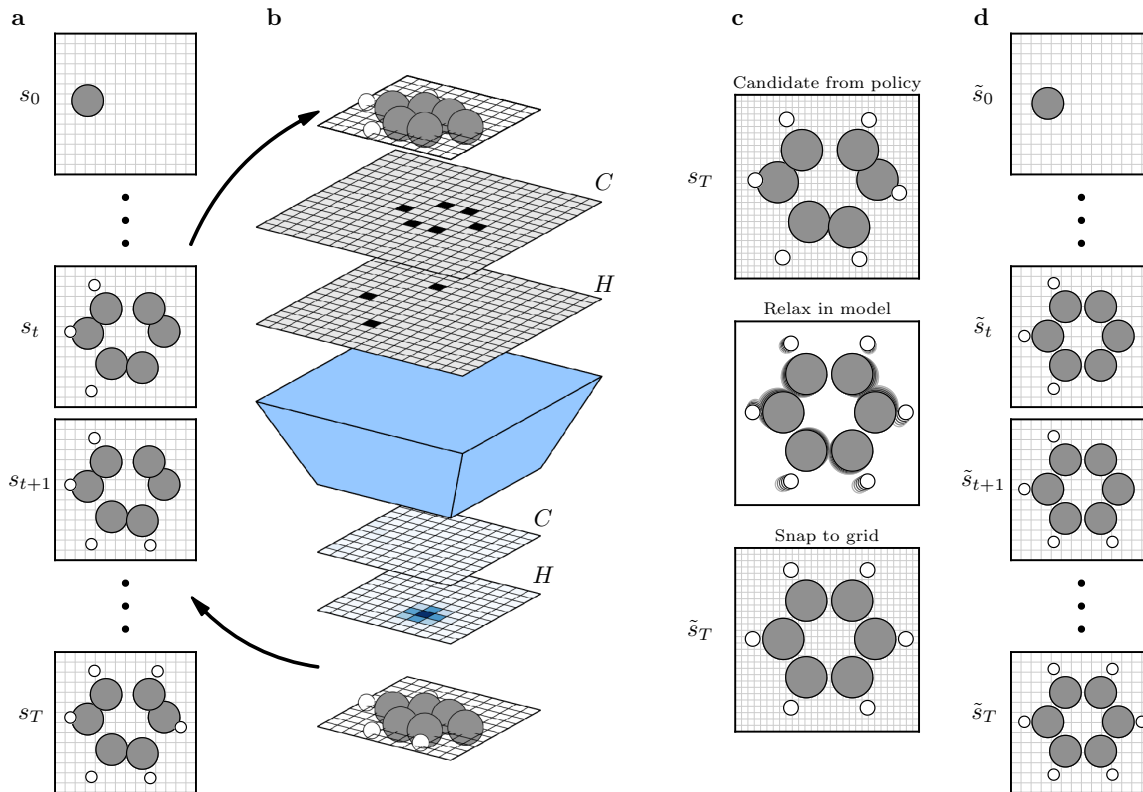


FIG. 2. **a** A candidate structure is constructed atom-by-atom in the *candidate-from-policy* operation by iteratively consulting a CNN (shown in **b**) and following the modified epsilon-greedy policy described in the text. This results in the sequence of structures,  $s_0, \dots, s_T$ . **c** The final structure,  $s_T$ , is relaxed in the surrogate energy model, resulting in the  $\tilde{s}_T$ -structure, for which the total energy is evaluated. **d** The  $\tilde{s}_T$ -structure is decomposed atom-by-atom to obtain the sequence,  $\tilde{s}_0, \dots, \tilde{s}_T$ , which is stored in the ASLA memory together with the energy, and used for training of both the CNN and the surrogate energy model.

date construction was proceeded by some relaxation, the state-action pairs will most likely deviate from the actual states,  $s_t$ , visited and actual actions,  $a_t$ , taken during the build action. Assuming, however, that atoms are placed in the same order, the state-action pairs,  $(\tilde{s}_t, \tilde{a}_t)$ , that would have led directly to the snapped, relaxed structure,  $\tilde{s}_T$ , can be determined, cf. Fig. 2 **d**, and stored with  $E_{\text{tot}}$  in the memory.

The reinforcement learning episode continues with a training phase, where the CNN and surrogate energy model are updated. The CNN is trained by first extracting a batch of state-action-energy pairs from the most recent, most-favorable and random episodes from the memory, such that the batch comprises  $5 \times N_{\text{atom}}$  state-action-energy pairs. The energies are transformed to reward values,  $r \in [-1, 1]$ , and the batch is expanded by rotated and mirrored versions of the state-action-energy pairs. The weights of the CNN are updated by a backpropagation step with a learning rate of  $10^{-3}$  that decreases the total mean squared error between the predicted value and the reward for state-action-energy pairs in the batch.

In the present work, we employ the same architecture for the neural network as in Refs.<sup>46,50,51</sup>. It is thus a convolutional neural network (CNN) with three hidden layers

and 10 kernels per layer, all with the leaky-ReLU activation function, except for the output, where a hyperbolic tangent function is applied. The structure is represented as a one-hot encoded matrix, which represents the  $xy$ - or  $xyz$ -coordinates in the first two or three dimensions, and the atom type in a final dimension. Penalizing terms are employed following Refs.<sup>46,50</sup>.

As a final operation during the learning phase of a reinforcement learning episode, an improved surrogate energy model is prepared for the next episode. This is done in the *train-surrogate-model* operation, which represents the final new element introduced to ASLA in this work. The surrogate energy model extracts from the memory  $(\tilde{s}_T, E_{\text{tot}})$  datapoints and constructs a structure-energy model. The details of the model are given in the next section.

Upon starting the reinforcement learning cycle, the neural network representing the agent can be initialized randomly meaning that ASLA learns completely autonomously from its interaction with the DFT program with no other input than the template,  $s_0$ , and the stoichiometry of the final structure,  $s_T$ . It may, however, benefit largely in a transfer learning setting, where network weights are inherited from a prior ASLA run solving a sim-

pler problem. Initially, before sufficient structure-energy datapoints have been collected and stored in memory, a sufficiently reliable surrogate model cannot be established, and the relax operation is simply skipped.

### III. SURROGATE MODEL

For the surrogate model, a Gaussian process (GP) regression model<sup>54</sup> is used. The model is trained on feature representations of the final structures and their total energies. The use of a feature representation means that the GP model incorporates e.g. rotational and translational energy invariances directly, unlike the CNN model used for the agent, which has to learn that via the applied data augmentation. The GP regression model, thus learns the underlying energy landscape more efficiently from the training data compared to what would be expected from using a CNN model. However, contrary to using a CNN for the  $Q$ -value map evaluation, using a GP model would be computationally expensive owing to the cost of evaluating the feature representation at every pixel in the map. It can therefore not form the basis for the policy guided building step in ASLA, where a CNN with its inexpensive image representation is preferred. A further reason why a CNN is preferred for the  $Q$ -value map prediction is that  $Q$ -values depend on the final structures that can be built from incomplete ones. Thus the  $Q$ -value evaluation must predict the consequences of future actions, something which is better done with the deep learning capabilities of the CNN.

A GP is specified by its prior mean,  $\mu(\mathbf{x})$ , and covariance function (the kernel),  $k(\mathbf{x}, \mathbf{x}')$ , which expresses the beliefs about the system prior to any observations. The training consists of inferring the posterior distribution, which takes into account the observed training data,  $\mathcal{D} = \{X, \mathbf{E}\}$ . The posterior can be analytically expressed due to the well-behaved marginalization properties of the GP. Namely, the posterior is also a GP with mean function given by

$$E(\mathbf{x}_*) = \mathbf{k}_*^T (K + \sigma_n^2 \mathbb{I})^{-1} [\mathbf{E} - \mu(\mathbf{x})] + \mu(\mathbf{x}). \quad (1)$$

where  $K = k(X, X)$  is the kernel matrix,  $\mathbf{k}_* = k(X, \mathbf{x}_*)$  and  $\sigma_n$  is a regularization hyperparameter that acts to prevent overfitting (we use  $\sigma_n = 3.2 \cdot 10^{-3}$ ). The posterior mean is taken as the model prediction of the energy. Computationally, the training is dominated by the inversion of the kernel matrix, which scales with the number of data points as  $\mathcal{O}(n^3)$ .

To take advantage of the rotational, translational and permutation symmetries of quantum chemistry, structures are represented by feature vectors that exhibit these symmetries. In this work, we choose the fingerprint descriptors of Oganov and Valle<sup>55</sup>.

The kernel is chosen to be a sum of two Gaussians with different length scales, similar to that proposed in<sup>56</sup>

$$k(\mathbf{x}, \mathbf{x}') = \theta_0 ((1 - \beta)e^{-|\mathbf{x} - \mathbf{x}'|^2 / 2\lambda_1^2} + \beta e^{-|\mathbf{x} - \mathbf{x}'|^2 / 2\lambda_2^2}) \quad (2)$$

where  $\mathbf{x}$  are the feature vectors and  $\theta_0$  is the maximal covariance. Using two length scales,  $\lambda_1$  and  $\lambda_2$ , improves the model by allowing the kernel to capture trends in a large, sparsely sampled configuration space, while maintaining resolution in smaller, more densely sampled regions. The prior mean is chosen to be a short-ranged repulsive potential, which is generally present between atoms. This naturally prohibits atoms to get too close during structure relaxations with the model, which may cause convergence problems when the total energy is evaluated. The feature vector is analytically differentiable with respect to the Cartesian coordinates, which allows us to obtain the predicted force according to the model. The relaxation is performed by iteratively moving the atoms based on the predicted force.

In training the model, the hyperparameters,  $(\theta_0, \lambda_1, \lambda_2)$ , are optimized by maximizing the log marginal likelihood<sup>57</sup>. For the training data, only the 500 lowest energy structures from the ASLA memory is used. This ensures that the model resolves the low-energy part of the configuration space, while keeping the computational training time small. No effort is thus made to capture high-energy structures in irrelevant parts of the configuration space.

The model is not meant to reproduce total energies with high accuracy. Rather, the purpose of the model is to guide ASLA into local minima of the configuration space in order to aid the global search. Therefore, we measure the models performance by the improvement in the number of ASLA episodes needed to solve a global optimization problem, instead of an error with respect to a test set.

### IV. BENZENE EXAMPLE

Having introduced to ASLA that candidates built from the policy may be relaxed in a surrogate energy landscape, we now turn to probe how it affects the overall performance of ASLA. In order to be able to make convincing statistics we choose to have ASLA solve the problem of building the most stable molecule given six carbon atoms and six hydrogen atoms, i.e.  $C_6H_6$ . The total energy expression is provided by a density functional based tight binding (DFTB) energy expression using the DFTB+ implementation<sup>58</sup>, since this provides a sufficiently accurate description that the correct chemical bonds are formed, yet at a much reduced computational cost compared to a DFT energy expression. As the solution turns out to be the planar molecule *benzene*, we address this problem with a 2D space. For this a grid spacing of 0.25 Å is used.

The performance of ASLA is gauged by restarting the structural search a great number of times with no data in the memory and with random initialization of the CNN. By compiling as a function of episode count, the share of search runs that have found the benzene molecule, we arrive at the success curves displayed in Fig. 3. The blue curve shows the performance of standard ASLA without

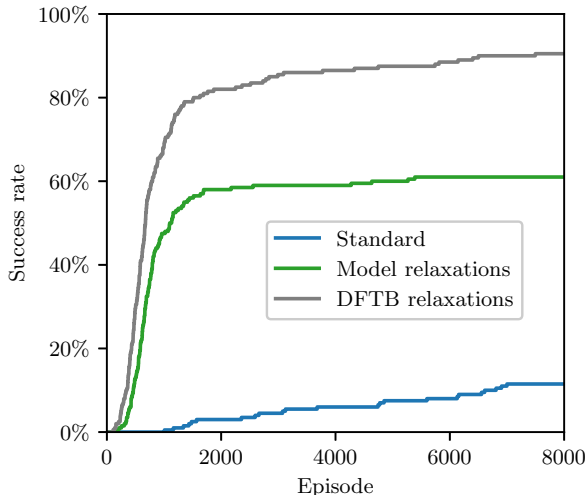


FIG. 3. Success curves based on 200 restarts. The standard ASLA (blue curve) is outperformed by ASLA augmented with model relaxations (green curve), without any additional energy evaluations. The grey curve shows the performance when DFTB relaxations are used in place of the model relaxations, imitating a perfectly trained model.

model relaxations, while the green curve shows the performance when the model relaxations are included. The here-proposed ASLA with model relaxations outperforms the standard ASLA by a wide margin. While standard ASLA needs  $\approx 7000$  episodes for 10% of the restarts to identify benzene, ASLA with model relaxations attains this after less than 1000 episodes.

The green success curve for the model-relaxed ASLA shows, however, one convergence issue. The fact that it levels off at about 60% success after about 2000 episodes means that the 40% of the restarts that have not found benzene within the first 2000 episodes stand a small chance of doing so in the remaining 6000 episodes of the runs. To probe the origin of this, we conducted a set of search runs, in which the relaxations of the policy-built candidate structures were done in the full DFTB energy landscape rather than with the on-the-fly learnt surrogate energy landscape. The grey curve in Fig. 3 shows the resulting success curve, which evidences that when relaxing candidates in the DFTB energy landscape, the stagnation almost vanishes. About 80% of the restarts have found benzene after 2000 episodes, and in the following 6000 episodes about half of the remaining restarts do so.

We consequently attribute the stagnation of the model-relaxed ASLA to errors in the surrogate energy model. Note, however, that the DFTB relaxation scheme uses several order of magnitudes more DFTB energy evaluations per episode, than does the model relaxation scheme, where one episode corresponds to one DFTB single-point energy evaluation. This renders the model relaxation scheme far superior when more refined and computationally expensive DFT or quantum chemistry methods are used as the total energy expression.

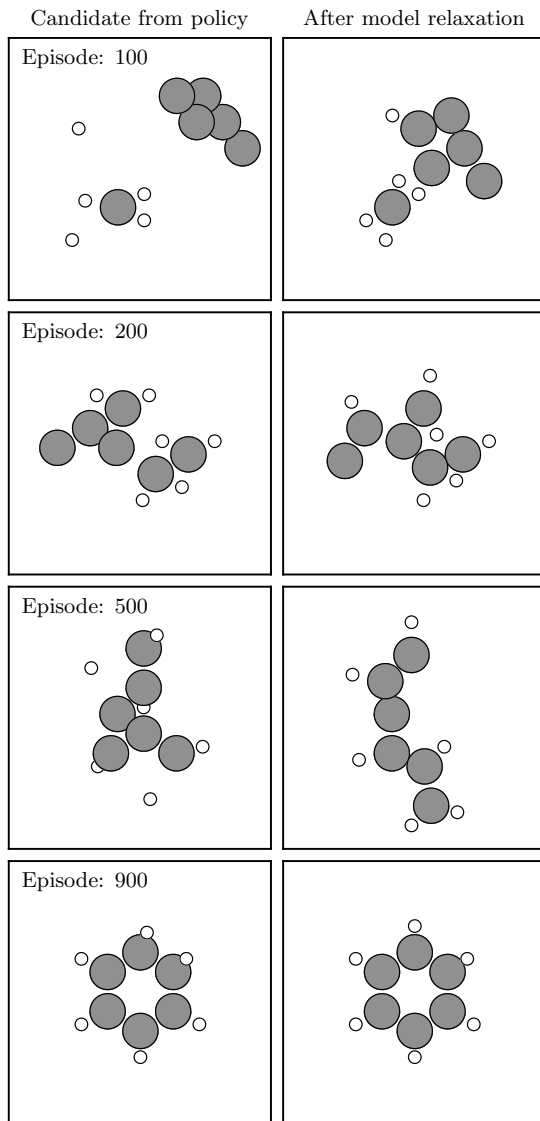


FIG. 4. The structures built according to the  $Q$ -value directed policy (left) and their appearance being relaxed in the model and snapped to the grid (right) for different stages of a search. The model potential quickly learns to locally optimize the structure that ASLA produces. In turn, ASLA learns more quickly to build stable structures (cf. Fig. 3).

Possible solutions to the stagnation issue could be the introduction of more advanced model energy expressions than the presently used one, or the development of schemes to reset the surrogate model upon detection of stagnation. Note that a single restart will not know if it has ceased to find better structures because it has identified the global minimum energy structure or because it uses an insufficiently accurate model for the relaxation and finds a higher lying energy structure. In practice, when searching for an unknown global minimum energy structure, all restarts would therefore need to have their model reset once they consistently produce the same best

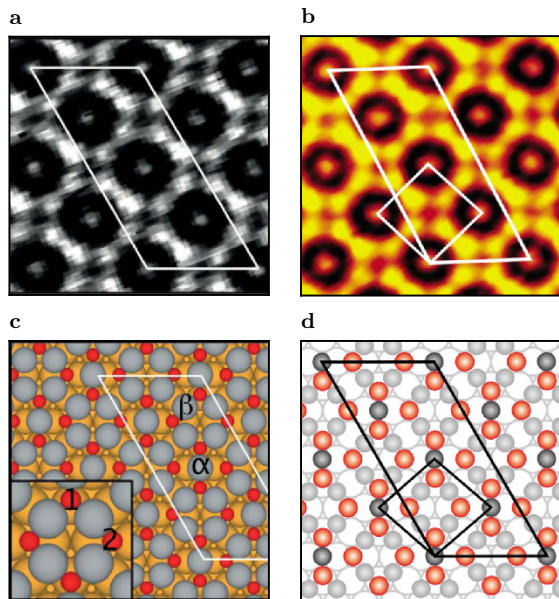


FIG. 5. The experimental STM images and conjectured atomistic structures. **a** and **c** reprinted with permission from Martin *et al* The Journal of Physical Chemistry C **118**, 15324 (2014). Copyright (2020) American Chemical Society. **b** and **d** adapted from Ref. 47.

structure over and over again.

Having seen that ASLA improves significantly upon adding the presently proposed model-relaxation, it is instructive to inspect the degree of relaxation as a function of reinforcement episodes. Figure 4 presents one such study for a randomly chosen restart. It shows the policy-built structure and the corresponding model-relaxed structure after 100, 200, 500, and 900 episodes. After 100 and 200 episodes, the agents CNN has not developed sufficiently yet as to consistently build molecules with chemical meaningful coordinations. However, the surrogate energy model has learnt enough to provide for relaxation of the atoms into having more proper interatomic distances. After 500 episodes, the policy-built structure still lacks a bit on C-C coordination and C-H bond lengths and it leaves some H as isolated atoms. All of these deficiencies are remedied by the model-relaxation and by 900 episodes, the agents starts to know how to build benzene in need of only very minor bond adjustments, mainly pertaining to the large grid spacing used. Note, that the CNN benefits from the improved training examples provided by the model relaxations, and learns to build reasonable structures faster than in the standard ASLA scheme.

## V. AG(111) OXIDE SURFACE

We now turn to apply ASLA with model relaxation to an outstanding problem in materials science. Specifically, we will be concerned with the oxidation of the Ag(111)-

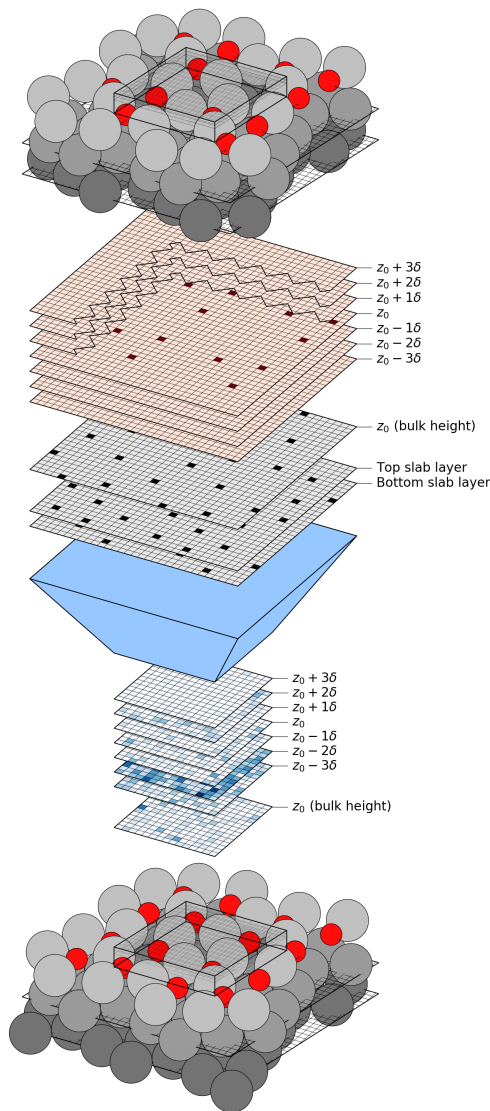


FIG. 6. The ASLA setup. Starting from above, an incomplete surface oxide structure on a two-layer Ag(111) template is shown. Red spheres are oxygen atoms, and grey spheres are silver atoms. The transparent box highlights the  $c(4 \times 8)$  unit cell. The two lowest layers of Ag atoms, two Ag(111) layers, are part of the template, while the upper most Ag atoms and all O atoms are being placed by ASLA. The convolutional neural network is fed with seven layers of allowed O positions (the brown grids) and with three layers of possible Ag positions (the grey grids). It outputs  $Q$ -values for all available oxygen atomic positions and for silver positions in the upper layer. In the final lower structure, an extra O atom has been added at the position of highest  $Q$ -value following a greedy policy.

surface, which has been shown to exhibit a rich variety of stoichiometries and phases during growth of surface oxide layers. Schnadt and co-workers<sup>47,48</sup> have reported scanning tunneling microscopy (STM) topographs of a number of such phases, one of which, the  $c(4 \times 8)$ -phase, is reproduced in Fig. 5. To the best of our knowledge,

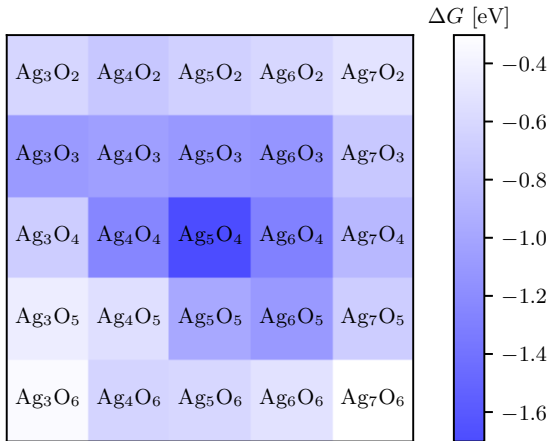


FIG. 7. Free energy,  $\Delta G$  evaluated at  $\Delta\mu_{\text{O}} = -0.5$  eV, for the most stable  $\text{Ag}(111)\text{-}c(4 \times 8)\text{-Ag}_X\text{O}_Y$  surface oxides found by ASLA.

no systematic structural search has been carried out for this particular surface oxide phase on  $\text{Ag}(111)$ , yet in the original paper a structural model was put forward<sup>47</sup>. By having ASLA perform the structural search given the experimentally determined surface unit cell, but covering a large range of Ag-O stoichiometries for the surface oxide, we confirm below the originally conjectured model in a set of ASLA runs.

In our search for the  $\text{Ag}(111)\text{-}c(4 \times 8)$  silver oxide phase, ASLA is used to identify the best possible structure of a mono-layer silver oxide on top of a bulk truncated  $\text{Ag}(111)$  template. For the surface oxide, it is assumed that all Ag atoms occupy positions whose heights coincide with that of an extra unrelaxed  $\text{Ag}(111)$  layer,  $z_0$ , while all O atoms occupy some of seven different heights evenly distributed around such a  $\text{Ag}(111)$  layer, i.e. ranging from 1.6 to 3.1 Å above the  $\text{Ag}(111)$  template. For the in-plane positions of the Ag and O atoms, any values on a 2D grid with grid spacing 0.255 Å are allowed. Figure 6 depicts these discretized positions as they are fed into the neural network. The seven brown layers hold the O atoms, while the three grey layers hold the Ag atoms. As a template of preplaced Ag atoms, the bottom two grey layers are prepopulated with two  $\text{Ag}(111)$  layers. The CNN, shown schematically as the blue polygon in Fig. 6, outputs  $Q$ -values for all oxygen layers and for the upper Ag layer as shown by the bluish raster plots in the figure. The network does not need to output any  $Q$ -values for the lower two Ag layers, since these are already fully occupied.

During the model relaxation the silver atoms are constrained to move in the  $xy$ -plane, while the oxygen atoms are constrained to move freely between  $z = 1.6$  Å and  $z = 3.1$  Å, which does not represent any further approximation given that the atomic position are snapped to the grid heights within these bounds at the end of the building phase.

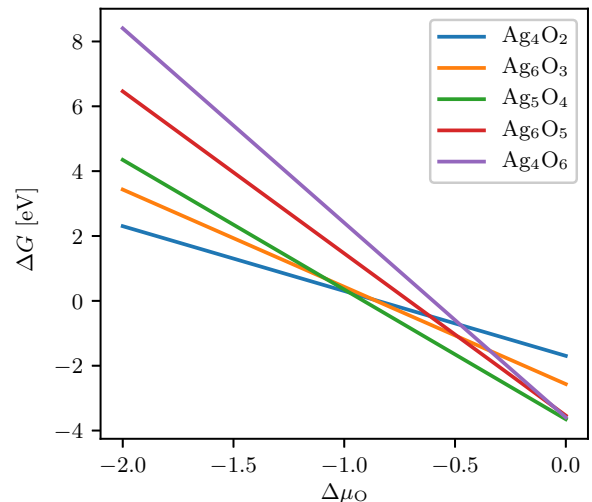


FIG. 8. Free energy,  $\Delta G$  as a function of  $\Delta\mu_{\text{O}}$  for the most stable  $\text{Ag}(111)\text{-}c(4 \times 8)\text{-Ag}_X\text{O}_Y$  surface oxides found by ASLA for  $Y = 2, 3, 4, 5$  and 6 when varying  $X$  from 3 to 7.

The evaluation phase is conducted using DFT. The structures are handled with the atomic simulation environment (ASE)<sup>59</sup> and the DFT based total energies are evaluated with the grid-based projector augmented wave package GPAW<sup>53</sup>. For the exchange-correlation functional, the Perdew-Burke-Ernzerhof (PBE) expression is used<sup>60</sup>.

ASLA was used to build  $\text{Ag}_X\text{O}_Y$  structures on top of  $\text{Ag}(111)\text{-}c(4 \times 8)$  for  $3 \leq X \leq 7$  and  $2 \leq Y \leq 6$ . For each combination of  $(X, Y)$  ASLA was restarted at least 10 times until the best structure found agreed in at least 5 of the restarts, except for some of the  $\text{Ag}_7\text{O}_Y$  runs, where only a few restarts agreed on the best structure before the allocated resources were spent. Once identified by ASLA, the best surface oxide structure ever found for each restart was transferred to 5 layered  $\text{Ag}(111)$  slabs and relaxed unconstrained. The structure and stability of these surface oxide models are discussed in the following.

We compare the different stoichiometries by their Gibbs free energy according to<sup>61</sup>:

$$\Delta G(T, p) = E^{\text{DFT}} - E_{\text{slab}}^{\text{DFT}} - X\mu_{\text{Ag}} - Y\mu_{\text{O}}(T, p), \quad (3)$$

where  $E^{\text{DFT}}$  is the DFT energy of the full structure,  $E_{\text{slab}}^{\text{DFT}}$  is the DFT energy of the  $\text{Ag}(111)\text{-}c(4 \times 8)$  five layer slab without the surface oxide, and where  $\mu_{\text{Ag}}$  and  $\mu_{\text{O}}$  are the chemical potentials of silver and oxygen, respectively. Note, that we neglect the small vibrational and configurational contributions to the Gibbs free energy of the surface structures. The silver chemical potential,  $\mu_{\text{Ag}}$ , is taken to be the chemical potential of a silver atom situated in the bulk position, calculated as the difference per Ag atom of 6 and 5 layer thick  $\text{Ag}(111)$  slabs. The oxygen chemical potential is a function of the di-oxygen

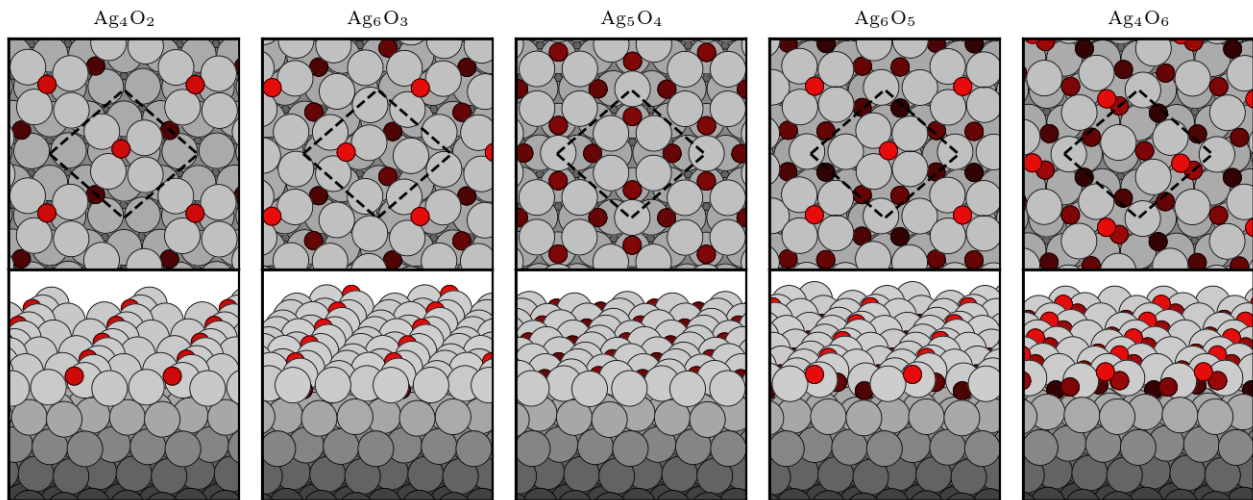


FIG. 9. Top and side view of the most stable  $\text{Ag}_X\text{O}_Y$  structures for each value of  $Y$  investigated in this work.

pressure,  $p$ , and the temperature,  $T$ <sup>61</sup>:

$$\mu_{\text{O}}(T, p) = \frac{1}{2} \left( E_{\text{O}_2}^{\text{DFT}} + \tilde{\mu}_{\text{O}_2}(T, p^0) + k_B T \ln \left( \frac{p}{p^0} \right) \right) \quad (4)$$

where  $E_{\text{O}_2}^{\text{DFT}}$  is the DFT total energy of the di-oxygen molecule,  $\tilde{\mu}_{\text{O}_2}(T, p^0)$  is the translational, rotational, and vibrational contributions to the free energy of an  $\text{O}_2$  gas at a reference pressure,  $p^0$ , and  $k_B$  is Boltzmann constant. It is seen that the absolute value of  $\mu_{\text{O}}(T, p)$  depends on the specific computational settings through  $E_{\text{O}_2}^{\text{DFT}}$ . To circumvent that, it is convenient to quote only the  $(T, p)$ -dependent part of the chemical potential:

$$\Delta\mu_{\text{O}}(T, p) = \mu_{\text{O}}(T, p) - \frac{1}{2} E_{\text{O}_2}^{\text{DFT}} \quad (5)$$

whenever a chemical potential is specified.

With the thermodynamic considerations in place, it is now possible to compare the stability of the most stable structures found by ASLA. Figure 7 does so in the form of a raster plot of the free energy,  $\Delta G$ , evaluated at an oxygen chemical potential of  $\Delta\mu_{\text{O}} = -0.5$  eV, corresponding approximately to ambient conditions, i.e. a pressure of 1 atm and a temperature of 300 K<sup>61</sup>. The plot shows a clear optimal stability for a surface oxide of  $\text{Ag}_5\text{O}_4$  stoichiometry, and it brings evidence that sufficient variation in the stoichiometry has been considered to call this the thermodynamic most stable state at this chemical potential for oxygen.

In Fig. 8 a diagram of the free energy as a function of  $\Delta\mu_{\text{O}}$  is shown. The diagram builds on the most stable  $\text{Ag}_X\text{O}_Y$  structure for every considered value of  $Y$ , i.e.  $\text{Ag}_4\text{O}_2$ ,  $\text{Ag}_6\text{O}_3$ ,  $\text{Ag}_5\text{O}_4$ ,  $\text{Ag}_6\text{O}_5$ , and  $\text{Ag}_4\text{O}_6$  surface oxides. The diagram shows that over a wide range of chemical potential for oxygen, the  $\text{Ag}_5\text{O}_4$  surface oxide remains the most stable.

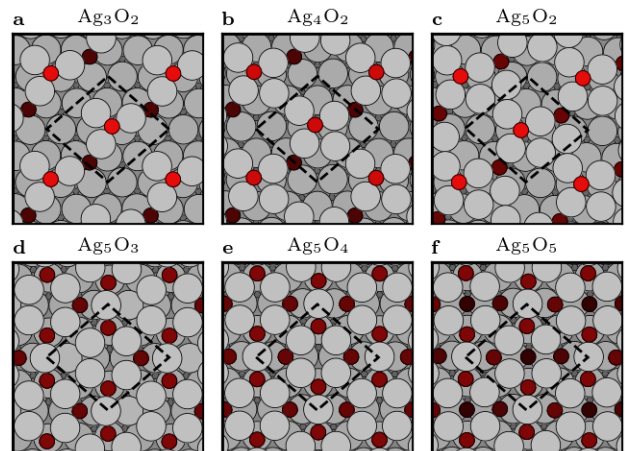


FIG. 10. Structures with similar motifs found for different stoichiometries. **a-c** show network-like structures for  $\text{Ag}_3\text{O}_2$ ,  $\text{Ag}_4\text{O}_2$  and  $\text{Ag}_5\text{O}_2$ . **d-f** show structures for  $\text{Ag}_5\text{O}_3$ ,  $\text{Ag}_5\text{O}_4$  and  $\text{Ag}_5\text{O}_5$ . Here, identical motifs are found for the Ag-atoms, while the oxygen sites are filled as more oxygen are introduced. Note that all structures above are found in separate, independent ASLA runs.

The structures leading to the free energy diagram in Fig. 8 are shown in Fig. 9. They expose a rich variety of chemical bonding motifs involving the Ag and O atoms within the surface oxide. Inspecting the structures in Fig. 9, the first one appears network type with voids, the next one resembles the first, but with reduced  $\text{Ag}_3$  islands in the voids, while the remaining three structures appear to have both Ag and O atoms highly dispersed in the surface oxide layer. As the oxygen content increases from left to right in the figure, ASLA eventually identifies the need for including  $\text{O}_2$  motifs when tasked with accommodating a large amount of oxygen within the surface oxide.

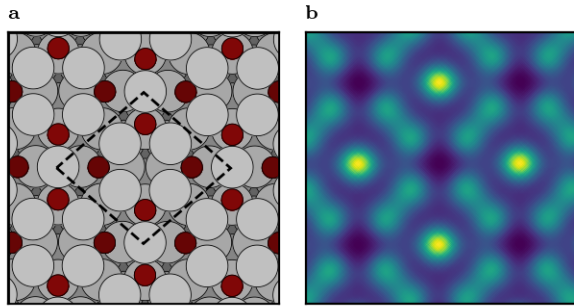


FIG. 11. **a** The  $\text{Ag}_5\text{O}_4$  structure and **b** the corresponding simulated STM image. The simulated STM agrees well with the experimental STM image (see Fig. 5 **a** and **b**).

The large diversity in the *optimal* structures shown in Fig. 9 testifies to ASLA's ability to identify a highly diverse set of chemically meaningful structures as the stoichiometry is varied. Conversely, collecting series of some of the *sub-optimal* structures found, it can be realized that ASLA often finds the same structural skeleton for different stoichiometries. This is illustrated in Fig. 10a-c, where it is seen that ASLA in independent searches for  $\text{Ag}_3\text{O}_2$  and  $\text{Ag}_5\text{O}_2$  stoichiometries finds again the optimal  $\text{Ag}_4\text{O}_2$  structure only with one Ag atom removed or added. Likewise, Fig. 10d-f shows how  $\text{Ag}_5\text{O}_3$  and  $\text{Ag}_5\text{O}_5$  structures are identified by ASLA that either lack one O or contain an extra O compared to the optimal

$\text{Ag}_5\text{O}_4$ . A full account of all structures found is given in the supplementary material.

Focusing on the  $\text{Ag}_5\text{O}_4$  surface oxide that we identify as the preferred structure, we note that ASLA has indeed found the same structure that was proposed by Schnadt *et al.*<sup>47</sup>. In Fig. 11 we present a Tersoff-Hermann type simulated STM topograph, that indeed matches the experimental STM one shown in Fig. 5. We thus conclude that ASLA with very little input (i.e. the surface unit cell and some choice for discretization of space) is capable of deducing the structure of a complicated surface oxide. It does so without requiring any human input of expected structural motifs or other presumed knowledge of chemical bonding within the surface oxide.

## VI. CONCLUSION

We have augmented ASLA with relaxations in a model potential, dramatically increasing the performance. The improvements come with no need for extra electronic-structure energy evaluations, and little overhead due to training the model and the relaxation procedure itself. We applied the improved ASLA to a  $\text{Ag}(111)$  oxide surface, where a proposed structure was confirmed by a thorough search.

## VII. ACKNOWLEDGEMENTS

We acknowledge support from VILLUM FONDEN (Investigator grant, Project No. 16562).

- 
- \* hammer@phys.au.dk
- <sup>1</sup> A. R. Oganov, C. J. Pickard, Q. Zhu, and R. J. Needs, *Nature Reviews Materials* **4**, 331 (2019).
  - <sup>2</sup> S. Kirkpatrick, C. D. Gelatt, and M. P. Vecchi, *Science* **220**, 671 (1983).
  - <sup>3</sup> D. J. Wales and J. P. K. Doye, *The Journal of Physical Chemistry A* **101**, 5111 (1997).
  - <sup>4</sup> B. Hartke, *The Journal of Physical Chemistry* **97**, 9973 (1993).
  - <sup>5</sup> D. M. Deaven and K. M. Ho, *Phys. Rev. Lett.* **75**, 288 (1995).
  - <sup>6</sup> A. R. Oganov and C. W. Glass, *The Journal of Chemical Physics* **124**, 244704 (2006).
  - <sup>7</sup> L. B. Vilhelmsen and B. Hammer, *Phys. Rev. Lett.* **108**, 126101 (2012).
  - <sup>8</sup> L. B. Vilhelmsen and B. Hammer, *The Journal of Chemical Physics* **141**, 044711 (2014).
  - <sup>9</sup> T. Ishikawa, T. Miyake, and K. Shimizu, *Phys. Rev. B* **100**, 174506 (2019).
  - <sup>10</sup> J. Schmidt, M. R. G. Marques, S. Botti, and M. A. L. Marques, *npj Computational Materials* **5**, 83 (2019).
  - <sup>11</sup> A. P. Bartók, M. C. Payne, R. Kondor, and G. Csányi, *Phys. Rev. Lett.* **104**, 136403 (2010).
  - <sup>12</sup> M. Rupp, A. Tkatchenko, K.-R. Müller, and O. A. von Lilienfeld, *Phys. Rev. Lett.* **108**, 058301 (2012).
  - <sup>13</sup> A. P. Bartók, R. Kondor, and G. Csányi, *Phys. Rev. B* **87**, 184115 (2013).
  - <sup>14</sup> J. Behler and M. Parrinello, *Phys. Rev. Lett.* **98**, 146401 (2007).
  - <sup>15</sup> K. T. Schütt, H. E. Sauceda, P.-J. Kindermans, A. Tkatchenko, and K.-R. Müller, *The Journal of Chemical Physics* **148**, 241722 (2018).
  - <sup>16</sup> J. S. Smith, B. T. Nebgen, R. Zubatyuk, N. Lubbers, C. Devereux, K. Barros, S. Tretiak, O. Isayev, and A. E. Roitberg, *Nature Communications* **10**, 2903 (2019).
  - <sup>17</sup> K. T. Schütt, M. Gastegger, A. Tkatchenko, K. R. Müller, and R. J. Maurer, *Nature Communications* **10**, 5024 (2019).
  - <sup>18</sup> H. Zhai, M.-A. Ha, and A. N. Alexandrova, *J. Chem. Theory Comput.* **11**, 2385 (2015).
  - <sup>19</sup> M. Todorović, M. Gutmann, J. Corander, and P. Rinke, *npj Computational Materials* **5**, 35 (2017).
  - <sup>20</sup> T. Yamashita, N. Sato, H. Kino, T. Miyake, K. Tsuda, and T. Oguchi, *Phys. Rev. Materials* **2**, 013803 (2018).
  - <sup>21</sup> G. Schmitz and O. Christiansen, *The Journal of Chemical Physics* **148**, 241704 (2018).
  - <sup>22</sup> V. L. Deringer, C. J. Pickard, and G. Csányi, *Phys. Rev. Lett.* **120**, 156001 (2018).
  - <sup>23</sup> V. L. Deringer, D. M. Proserpio, G. Csányi, and C. J. Pickard, *Faraday Discuss.* **211**, 45 (2018).
  - <sup>24</sup> Q. Tong, L. Xue, J. Lv, Y. Wang, and Y. Ma, *Faraday Discussions* **211**, 31 (2018).

- <sup>25</sup> K. Gubaev, E. Podryabinkin, G. Hart, and A. Shapeev, *Comput. Mater. Sci.* **156**, 148 (2019).
- <sup>26</sup> M. Van den Bossche, *J. Phys. Chem. A* **123**, 3038 (2019).
- <sup>27</sup> J. S. Smith, B. Nebgen, N. Lubbers, O. Isayev, and A. E. Roitberg, *J. Chem. Phys.* **148**, 241733 (2018).
- <sup>28</sup> L. Zhang, D.-Y. Lin, H. Wang, R. Car, and W. E, *Physical Review Materials* **3**, 023804 (2019).
- <sup>29</sup> E. L. Kolsbjerg, A. A. Peterson, and B. Hammer, *Phys. Rev. B* **97**, 195424 (2018).
- <sup>30</sup> Z. Li, J. R. Kermode, and A. De Vita, *Phys. Rev. Lett.* **114**, 096405 (2015).
- <sup>31</sup> A. A. Peterson, R. Christensen, and A. Khorshidi, *Phys. Chem. Chem. Phys.* **19**, 10978 (2017).
- <sup>32</sup> K. Miwa and H. Ohno, *Phys. Rev. Materials* **1**, 053801 (2017).
- <sup>33</sup> E. V. Podryabinkin and A. V. Shapeev, *Comput. Mater. Sci.* **140**, 171 (2017).
- <sup>34</sup> R. Jinnouchi, F. Karsai, and G. Kresse, *Phys. Rev. B* **100**, 014105 (2019).
- <sup>35</sup> N. Bernstein, G. Csányi, and V. L. Deringer, *npj Computational Materials* **5**, 99 (2019).
- <sup>36</sup> O.-P. Koistinen, F. B. Dagbjartsdóttir, V. Ásgeirsson, A. Vehtari, and H. Jónsson, *J. Chem. Phys.* **147**, 152720 (2017).
- <sup>37</sup> E. Garijo del Río, J. J. Mortensen, and K. W. Jacobsen, *Phys. Rev. B* **100**, 104103 (2019).
- <sup>38</sup> M. S. Jørgensen, U. F. Larsen, K. W. Jacobsen, and B. Hammer, *The Journal of Physical Chemistry A* **122**, 1504 (2018).
- <sup>39</sup> M. Todorović, M. U. Gutmann, J. Corander, and P. Rinke, *npj Computational Materials* **5**, 35 (2019).
- <sup>40</sup> M. S. Jørgensen, M. N. Groves, and B. Hammer, *Journal of Chemical Theory and Computation* **13**, 1486 (2017).
- <sup>41</sup> T. L. Jacobsen, M. S. Jørgensen, and B. Hammer, *Phys. Rev. Lett.* **120**, 026102 (2018).
- <sup>42</sup> X. Chen, M. S. Jørgensen, J. Li, and B. Hammer, *Journal of Chemical Theory and Computation* **14**, 3933 (2018).
- <sup>43</sup> S. A. Meldgaard, E. L. Kolsbjerg, and B. Hammer, *The Journal of Chemical Physics* **149**, 134104 (2018).
- <sup>44</sup> S. Chiriki, M.-P. V. Christiansen, and B. Hammer, *Phys. Rev. B* **100**, 235436 (2019).
- <sup>45</sup> K. H. Sørensen, M. S. Jørgensen, A. Bruix, and B. Hammer, *The Journal of Chemical Physics* **148**, 241734 (2018).
- <sup>46</sup> M. S. Jørgensen, H. L. Mortensen, S. A. Meldgaard, E. L. Kolsbjerg, T. L. Jacobsen, K. H. Sørensen, and B. Hammer, *The Journal of Chemical Physics* **151**, 054111 (2019).
- <sup>47</sup> J. Schnadt, J. Knudsen, X. L. Hu, A. Michaelides, R. T. Vang, K. Reuter, Z. Li, E. Lægsgaard, M. Scheffler, and F. Besenbacher, *Phys. Rev. B* **80**, 075424 (2009).
- <sup>48</sup> N. M. Martin, S. Klacar, H. Grönbeck, J. Knudsen, J. Schnadt, S. Blomberg, J. Gustafson, and E. Lundgren, *The Journal of Physical Chemistry C* **118**, 15324 (2014).
- <sup>49</sup> A. Michaelides, K. Reuter, and M. Scheffler, *Journal of Vacuum Science & Technology A* **23**, 1487 (2005), <https://doi.org/10.1116/1.2049302>.
- <sup>50</sup> S. A. Meldgaard, H. L. Mortensen, M. S. Jørgensen, and B. Hammer, *Journal of Physics: Condensed Matter* **32**, 404005 (2020).
- <sup>51</sup> M.-P. V. Christiansen, H. L. Mortensen, S. A. Meldgaard, and B. Hammer, Submitted to *J. Chem. Phys.*
- <sup>52</sup> J. J. Mortensen, L. B. Hansen, and K. W. Jacobsen, *Phys. Rev. B* **71**, 035109 (2005).
- <sup>53</sup> J. Enkovaara, C. Rostgaard, J. J. Mortensen, J. Chen, M. Dulak, L. Ferrighi, J. Gavnholt, C. Glinsvad, V. Haikola, H. A. Hansen, H. H. Kristoffersen, M. Kuisma, A. H. Larsen, L. Lehtovaara, M. Ljungberg, O. Lopez-Acevedo, P. G. Moses, J. Ojanen, T. Olsen, V. Petzold, N. A. Romero, J. Stausholm-Møller, M. Strange, G. A. Tritsaridis, M. Vanin, M. Walter, B. Hammer, H. Häkkinen, G. K. H. Madsen, R. M. Nieminen, J. K. Nørskov, M. Puska, T. T. Rantala, J. Schiøtz, K. S. Thygesen, and K. W. Jacobsen, *Journal of Physics: Condensed Matter* **22**, 253202 (2010).
- <sup>54</sup> C. E. Rasmussen and C. K. I. Williams, *Gaussian Processes for Machine Learning* (The MIT Press, 2005).
- <sup>55</sup> A. R. Oganov and M. Valle, *The Journal of Chemical Physics* **130**, 104504 (2009).
- <sup>56</sup> M. K. Bisbo and B. Hammer, *Phys. Rev. Lett.* **124**, 086102 (2020).
- <sup>57</sup> C. E. Rasmussen and C. K. I. Williams, *Gaussian Processes for Machine Learning* (The MIT Press, 2005).
- <sup>58</sup> B. Aradi, B. Hourahine, and T. Frauenheim, *The Journal of Physical Chemistry A* **111**, 5678 (2007).
- <sup>59</sup> A. H. Larsen, J. J. Mortensen, J. Blomqvist, I. E. Castelli, R. Christensen, M. Duak, J. Friis, M. N. Groves, B. Hammer, C. Hargus, E. D. Hermes, P. C. Jennings, P. B. Jensen, J. Kermode, J. R. Kitchin, E. L. Kolsbjerg, J. Kubal, K. Kaasbjerg, S. Lysgaard, J. B. Maronsson, T. Maxson, T. Olsen, L. Pastewka, A. Peterson, C. Rostgaard, J. Schiøtz, O. Schütt, M. Strange, K. S. Thygesen, T. Vegge, L. Vilhelmsen, M. Walter, Z. Zeng, and K. W. Jacobsen, *J. Phys. Condens. Matter* **29**, 273002 (2017).
- <sup>60</sup> J. P. Perdew, K. Burke, and M. Ernzerhof, *Phys. Rev. Lett.* **77**, 3865 (1996).
- <sup>61</sup> K. Reuter and M. Scheffler, *Phys. Rev. B* **68**, 045407 (2003).